Electromagnetic Steering of Sodium-Seeded Rocket Thrust Plumes: Design & Analysis

by

Levi Gershon

Submitted to the
Department of Mechanical Engineering
in Partial Fulfillment of the Requirements for the Degree of

Bachelor of Science in Mechanical Engineering

at the

Massachusetts Institute of Technology

February 2023

Authored by: Levi Gershon
Department of Mechanical Engineering
January 18th, 2023

Certified by: Douglas Hart
Professor of Mechanical Engineering
Thesis Supervisor

Accepted by: Kenneth Kamrin
Professor of Mechanical Engineering
Undergraduate Officer

Electromagnetic Steering of Sodium-Seeded Rocket Thrust Plumes: Design & Analysis

by

Levi Gershon

Submitted to the Department of Mechanical Engineering
on **January 18, 2023** in Partial Fulfillment of the
Requirements for the Degree of

Bachelor of Science in Mechanical Engineering

ABSTRACT

This paper explores the use of the Lorentz force to magnetically steer a rocket engine's thrust plume, creating an off-axis thrust component. The perpendicular force component thus generated, for the sample design used is estimated at **0.002%** without sodium seeding, and **3.5%** with said seeding. The design of a prototype thruster is undertaken, burning gaseous propane and oxygen, resulting in a combustion chamber, expansion nozzle, and a magnetic circuit to drive the Lorentz steering force. While the predicted unseeded effect is too small to be useful, sodium seeding may be viable on small vehicles or satellites where minimizing overall system complexity is benefited by eliminating otherwise separate attitude control systems.

Thesis Supervisor: Douglas Hart
Title: Professor of Mechanical Engineering

Acknowledgments

This thesis would not have been possible without the assistance of numerous people and organizations across MIT, and while no list like this can be exhaustive, I shall endeavor to acknowledge the many people who gave time and resources to make this possible.

To all those who work tirelessly within the Edgerton Center, supporting student teams and projects, thank you: in particular, thank you to Kim Vandiver, for providing inspiration, funding, and access to equipment; to Sandra Liponski, who so deftly purchased the needed supplies; to James Bales, for his advice with instrumentation and safety; and to Pat McAtamney, for running the N51 machine shop and providing machining guidance for unusual materials.

Relatedly, thank you to the MIT Motorsports team, itself supported by the Edgerton Center, and to its many members for providing space and infrastructure. While this thesis is not directly contributing to that team's racecar, it is in many ways shaped by my experience thereon, from my familiarity with complex machining for that team, to safety-conscious design, and the art of using analytic formulas for mechanical design. I will forever be grateful for the opportunity afforded to me as a member of MIT Motorsports, and to my peers, whose combined efforts made it such a formative environment.

Additionally, I want to express my gratitude towards the many professors I consulted to shape this project. My thanks to Professor Jeffrey Lang, for his help in devising the magnetic flux concentration circuit used, and tireless discussions of all phenomena magnetic. Likewise, my thanks to Professor Carmen Geurra-Garcia, without whose input the plume analysis would not have been possible. Special appreciation is owed to Professor Paulo Lozano, whose detailed notes on rocket design provided much of the analytical basis used here, and who helped guide me through the complexities of the chemical calculations needed.

Finally, I owe immense gratitude to the two people who most directly enabled this work. To my advisor, both for this project and through my time at MIT, Douglas Hart, thank you for having faith in me throughout. From an unconventional academic journey to visions of strange devices, this one among them, you have made things possible I thought would remain only dreams. To Aaron Becker, my peer and dear friend, who followed me first onto MIT Motorsports and then

into working on magnetic rockets, thank you. Your trust means the world to me, and your feedback and tireless engagement as my sounding board have made this possible. You've devised the control board for this rocket, the brains to fire it, and I look forward to doing just that with you, and watching our combined projects spit fire together.

TABLE OF CONTENTS

Abstract 3
Acknowledgments **5**
1. Introduction **11**
1.1 Rocket Engine Operation 11
1.2 Existing Steering Technologies 12
1.3 Magnetically Steered Thruster Overview 13
1.4 Prototype Design Process & Requirements 15
2. Combustion Chamber **17**
2.1 Propellant Supply System 17
2.2 Combustion Theory 19
2.3 Chemical Analysis 21
2.4 Combustion Chamber Design 21
3. Flow Acceleration Nozzle **25**
3.1 Nozzle Theory 25
3.2 Nozzle Parameters 27
3.3 Nozzle Thermal Analysis 29
4. Magnetic Plume Steerage **34**
4.1 Steering Force Analysis 34
4.2 Magnetic Circuit Design 37
5. Conclusion **40**
5.1 Future Work 40
6. Bibliography **42**
Appendix **44**
A. Variable Names 44
B. CEA Script 47

List of Figures

Figure 1.1:	Rocket ΔV Diagram	11
Figure 1.2:	Rocket Components Schematic	12
Figure 1.3:	Top Level Assembly, Isometric View	15
Figure 2.1:	Propellant Supply Pneumatic Diagram	18
Figure 2.2:	Combustion Chamber Schematic	20
Figure 2.3:	Combustion Chamber, Cross Section	22
Figure 2.4:	Combustion Chamber, Isometric View	23
Figure 3.1:	De Laval Nozzle Diagram	25
Figure 3.2:	Nozzle, Cross Section	28
Figure 3.3:	Nozzle Thermal Circuit Model	29
Figure 4.1:	Magnetic Circuit, Orthogonal View	37
Figure 4.2:	Magnetic Circuit Model	38

1. Introduction

1.1 Rocket Engine Operation

Fundamental to this project is the chemical rocket, where combustion energy is used to accelerate propellant mass and create thrust. To model the performance of a chemical rocket engine, it is valuable to first consider the dynamics of a simplified rocket. It is typical for first-order analysis to assume that the relative velocity of the exhaust to the engine is constant, and represented by c, as in **Figure 1.1**. From momentum conservation principles, the Tsiolkovsky rocket equation can be found, shown in **Equation 1.1**, relating the change in velocity imparted on the rocket to the change in mass, m_0/m_f, and the exhaust velocity, c. [1]

$$\Delta v = c \ln \frac{m_0}{m_f} \tag{1.1}$$

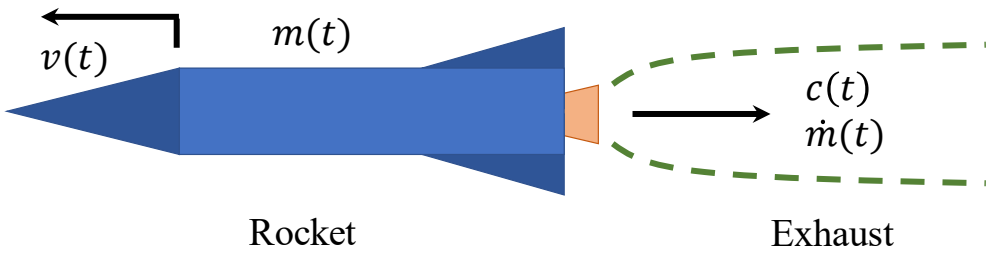

Figure 1.1: Diagram showing a rocket moving leftward, accelerating due to exhaust with velocity $c(t)$, engine flow rate $\dot{m}(t)$, rocket mass $m(t)$, and forward velocity $v(t)$.

Notably, while the logarithmic term in **Equation 1.1** forms a sharp law of diminishing returns on increased fuel expenditure, the change in velocity is linear with the exhaust velocity. The exhaust velocity is thus an effective basic measure of performance, and is commonly reported as such for engine design, in terms of the specific impulse, I_{sp}, defined in terms of the exhaust velocity by **Equation 1.2** [2].

$$I_{sp} = \frac{c}{g} \tag{1.2}$$

Next, considering the operation of the engine itself, a typical structure for a liquid or gas engine is that indicated in **Figure 1.2.** A combustion chamber, into which the fuel and oxidizer are

sprayed, mixed, and ignited, is connected to a converging-diverging nozzle which supersonically accelerates the resulting hot gas. The principles underlying these two components will be discussed in further detail in **Section 2.1** for the combustion chamber and **Section 3.1** for the nozzle. While practical rockets require powerful pumps to feed propellant at sufficient rates, and complex cooling due to the high heat fluxes generated, such systems are not directly relevant to the thrust steerage of this paper, and are thus not considered further here [3].

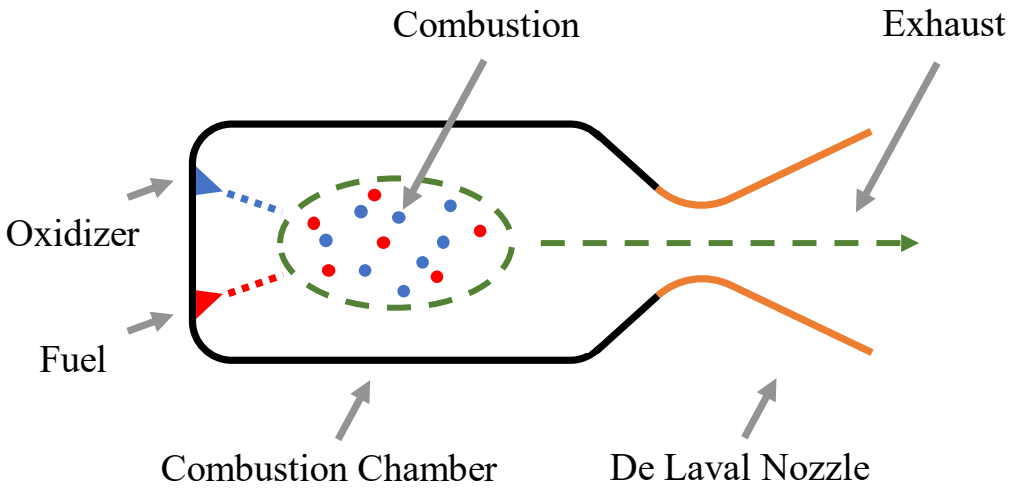

Figure 1.2: Cross-sectional simplified schematic of a typical chemical rocket. Oxidizer and fuel are injected into the combustion chamber, mixed carefully, allowed to isobarically expand, and then accelerated through the converging-diverging (de Laval) nozzle to produce thrust.

1.2 Existing Steering Technologies

In order to control the attitude of such rocket-propelled vehicles, both against external perturbations and towards a desired trajectory, a steering system with a high moment capability is needed. Often, this steering system in some way uses the thrust of the rocket engines providing the acceleration, and is then known as thrust-vector control (TVC). Numerous schemes have been devised and implemented for such a mechanism: a common solution is to gimbal the entire engine assembly, as was done with the Space Shuttle RS-25 main engines [3]. These often have gimbaling ranges of around 5°, such as was the case for F1 engines on the Saturn V, resulting in approximately 9% of the thrust vector perpendicular to the centerline [4]. Other options implemented include movable carbon vanes, inserted into the flow to deflect the plume, or entire secondary thrust chambers, called vernier thrusters [2]. Unfortunately gimbaling, vanes, and

vernier thrusters all involve substantial additional components and thus introduce undesirable weight and complexity.

One possible alternative is the use of fluid injection into the nozzle, called fluidic thrust vector control, to instead use asymmetric hydrodynamic effects to achieve steering. This technology has been analyzed by many [5–7], and was even implemented on the Cold War-era Lance missile, which used pulses of fuel injected into the sides of the engine nozzle to provide TVC [3]. More recently, Lee et al. constructed such a system for use with a hybrid motor[1] with some success, but required as much as 9% of the total flow to be through the side injectors [8]. Indeed, the testing done by Zmijanovic et al., among others, reveals significant complexities with this approach due to chaotic shock waves [9]. While the NASA Langley Research Center has investigated various strategies to mitigate these chaotic effects, including counterflow in the nozzle and shifting the engine throat, with some success, these strategies nevertheless come at a cost to the rocket's efficiency [5].

The final engine steering technology possible is to use electromagnets to guide the exhaust, allowing a solid-state, lightweight mechanism to be used instead of heavy gimbals. Such a concept was proposed by David Fearn in 2001 for use with electric thrusters, since the entirely ionized exhaust from such engines is easily amenable to Lorentz steering [10]. Then, in 2019, Edamato et al. successfully built such a magnetically steered ion thruster [11]. Finally, and most directly related to this project, although no detailed analysis was published with it, a patent was filed in 2019 by Chao Huo for the use of magnetic coils to deflect the thrust from a solid rocket based on its exhaust's partial ionization [12]. That patent did not consider the usability of the magnetic steering for liquid rocket engines; that analysis and the design of a test setup are the subject of this paper.

1.3 Magnetically Steered Thruster Overview

In order to create a magnetic force – and thus to achieve magnetic thrust vector control – the presence of moving charges is needed, as indicated by the Lorentz force law in **Equation 1.3** [13].

$$\vec{F}_{\perp} = \vec{J} \times \vec{B} \tag{1.3}$$

[1] One which operates using a solid fuel and a liquid oxidizer, similar to the concept discussed in **Section 1.1** but with a somewhat different combustion chamber.

At first appraisal, there is no net current acting over the exhaust plume, or even many ions to carry a charge. However, due to differences in the collisionality between ionized molecules and electrons, a pseudo-current can be considered to exist, where the electrons are accelerated rapidly and thus absorb little momentum, while the cations collide with un-ionized gas molecules and provide a net momentum transfer. The details of this analysis are pursued in **Section 4.1**, but the principle is enough to shape the parameters for a prototype magnetically steered engine. Since the physics underlying this proposed phenomenon are somewhat uncertain, especially in the presence of the complex flow scenario of a rocket engine, a prototype is needed.

The design of that prototype is undertaken here, with the aim of determining the validity of magnetic steering technology for use with chemical rocket engines. **Figure 1.3** shows the design of that prototype, implemented as the minimum scope needed to create a realistic operating regime. Using propane and oxygen gas, fed from pressurized tanks and ignited via an automotive spark plug, the combustion mixture flows into a stainless-steel converging-diverging nozzle. Wrapped around that nozzle is an electromagnetic circuit, concentrating the flux generated by a solenoid to the throat of the engine. This results in an effective magnetic flux density within the throat of 710 mT. While without alkaline seeding, the steering effect is likely non-existent – predicted as 0.002% of the total thrust – this can be increased dramatically with small quantities of a sodium salt. Upon the addition of merely 0.5% sodium by mass to the fuel mixture, the thrust steerage grows to 3.5%. The details of the design shall be explored in the sections below, discussing first the combustion chamber in **Section 2**, then the expansion nozzle in **Section 3**, and the magnetic circuit and plume steerage in **Section 4**.

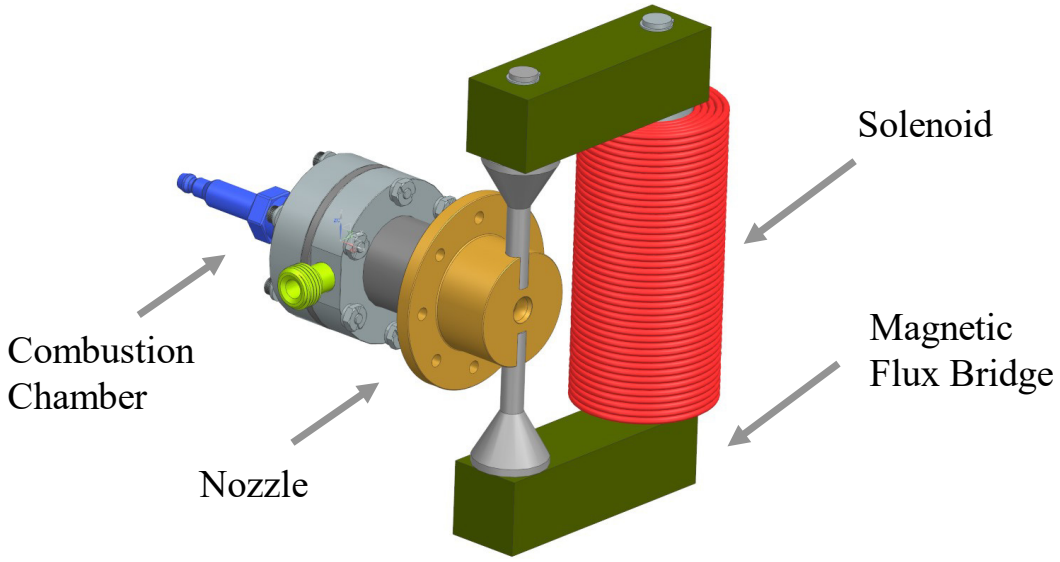

Figure 1.3: Isometric view of prototype rocket and steering coil assembly CAD, with key elements labeled.

1.4 Prototype Design Process & Requirements

In order to convert the vast design space of rocketry into a useful prototype, design requirements and process methodology had to be formulated. **Table 1.1** summarizes the core requirements for the engine assembly design. Foremost, it must evaluate the proposal, namely, to use Lorentz steering for thrust vector control. In order to be applicable to rocketry, it must emulate typical flow parameters, per the second requirement in **Table 1.1**; size is not an immediate factor. Then, it must apply a strong magnetic field to the flow, lest the effect of a small magnetic be overwhelmed by other concerns. To be competitive with existing solutions, the flow redirection must be of comparable order of magnitude to that from gimbaled solutions, set to a target of 1% in requirement 4. As with any piece of hardware, the constraints of the manufacturing capabilities and budget available must be obeyed, namely requirement 5, in this requiring case that the engine must be manufacturable within the vertical milling and turning machines available at MIT. Additionally, due to the inherent danger of explosive failure in rocketry, safety to both the users and to the equipment for successful operation must be articulated as a requirement. This requirement for safety in turn drove the overall size of the equipment, constraining pressures and flow rates to the levels selected. Finally, it is chosen to target a half minute firing period to permit for simple instrumentation and control, avoiding high frequency data collection.

Table 1.1: Engine Assembly Design Requirements	
1	Evaluate the feasibility of using Lorentz force steering for rocket engine thrust vector control
2.	Emulate typical rocket engine flow parameters
3.	Apply a high magnetic field to exhaust
4.	Provide a perpendicular thrust component at least 1% of the total thrust
5.	Achieve system manufacturability within MIT on-campus capabilities
6.	Maintain system safety to equipment and user
7.	Allow for a 30s firing period

Since the system requirements do not desire optimization for any specific application, a design methodology focusing on achieving a functional product was chosen. Where parameter sensitivity sweeps and extensive analysis might typically be conducted, for this prototype only the minimal analysis of a manufacturable set of parameters was done. Analysis was restricted to the use of analytic formulas and existing chemistry tools, but was used to ensure safe performance to the greatest extent possible. By accelerating the design process in this way, rapidly arriving upon a prototype, empirical results will be obtained quickly to permit more optimal subsequent iterations.

2. Combustion Chamber

To provide the energy used to accelerate the propellant in the rocket engine, chemical combustion is used. That combustion occurs within the combustion chamber, described below, and requires the gas to be rapidly fed into the chamber. The combustion chamber must then ensure proper mixing of the fuel and oxidizer, as well as ignition, while also resisting the extreme temperatures thus developed. The propellant supply system, largely determined by considerations of safety, is discussed first in **Section 2.1**, and then background for the analysis used to size that chamber is elucidated in **Section 2.2**, along with the underlying chemical analysis in **Section 2.3,** followed by the details of the actual architecture implemented in **Section 2.4**.

2.1 Propellant Supply System

In order to determine the overall system size, the target flow rates and thrust had to be determined. Since there is no distinct design requirement for the magnitude of thrust, the desired flow rate is instead limited by considerations of safety. To avoid the deadly danger of blowback – a phenomenon where the flame front traverses back through the feedlines and detonates the gas supply – it was chosen to limit the flow rates and pressures to those within the capabilities of commercial cutting torch flashback arrestors. Rated to ensure both gas non-return and flame arrest, these provide the first line of safety for the prototype envisioned. In so doing, they also limit the mass flow and pressures developed. Additional safety measures developed within the feed system include normally-closed shutoff valves, to ensure system failure results in combustion termination, and temperature, pressure, and leakage termination conditions, which fell within the design scope of Aaron Becker's work and shall be discussed by him in a separate paper. These safety systems, taken together, are shown in the system pneumatic diagram in **Figure 2.1**, which provides a qualitative view of the propellant supply.

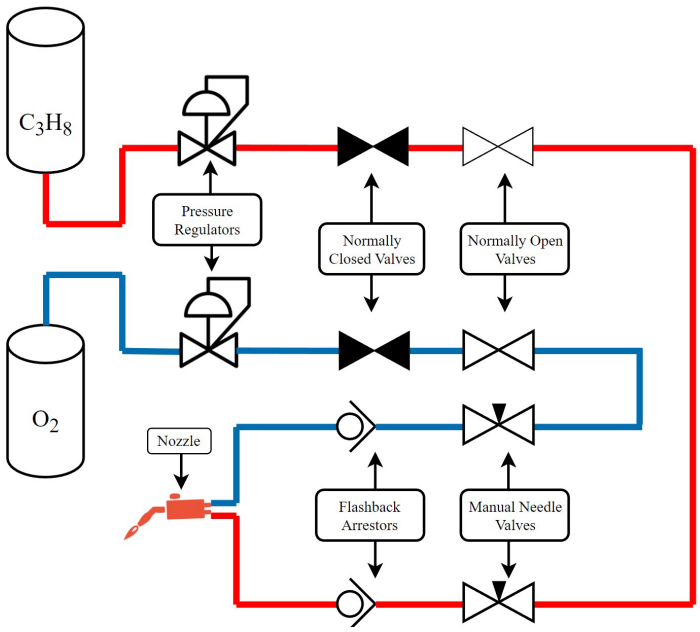

Figure 2.1: System pneumatic diagram, showing flow control valves from the tank regulators to the nozzle. Regulators control the output pressure from the tank, then moderated by the normally closed valves, the computer firing valves, and the needle control valves. While the flashback arrestors also act as check valves, it may be necessary to add separate check valves. A nitrogen purge system was omitted due to the low volume of gases present in the system; subsequent testing may countermand this decision.

Next, oxygen and propane were chosen as the combustion gases due to their easy commercial availability. Maximizing the combustion pressure within the constraint of flashback arrestors available on McMaster-Carr, the gauge pressure in the feed lines is chosen at 312 kPa (45.3 psi) [14]. The gas lines used are 6.35mm (0.25in) in diameter, and are assumed to be long and isothermal. This then sets the combustion pressure as the absolute pressure of the feed lines, minus the pressure drop due to the valves and injection orifices.

Assuming then that the flow is isothermal and isentropic, the flow rate through the feed lines is given by **Equation 2.1**, dependent on an uncertain discharge coefficient C_D, assumed to be 0.7, as well as on the orifice area A_{hose}, input pressure and temperature, P_{in} and T_{in}, and chamber pressure P_0 [15].

$$\dot{m}_{hose} = C_D A_{hose} P_0 \sqrt{\frac{1}{RT_{in}} \frac{2\gamma}{\gamma - 1} \left(\frac{P_0}{P_{in}}\right)^{\frac{2}{\gamma}} \left(1 - \left(\frac{P_0}{P_{in}}\right)^{\frac{\gamma-1}{\gamma}}\right)} \quad (2.1)$$

Computed for room temperature oxygen and propane, this result in a maximum flow rate for the oxygen gas of 21.73 g/s when sonically choked. Balancing pressure lost from combustion against increased mass flow, as well as manufacturability concerns, it was chosen to target an oxygen mass flow of 8.05 g/s, resulting in an absolute combustion pressure of 400,000 kPa (58 psi).

Next, to achieve the proper mass ratios, the oxygen mass flow rate must be matched to the propane flow to achieve the ideal molar ratio. **Equation 2.2** shows the stoichiometric combustion reaction for oxygen and propane, with a ratio of 5 moles of oxygen for each mole of propane burned. This matching is to be accomplished via decreasing the injector hole diameter for the fuel ports, since it is the oxygen flow that is the limiting reactant.

$$C_3H_8 + 5O_2 \rightarrow 4H_2O + 3CO_2 \quad (2.2)$$

Accordingly, it is expected that to match the oxygen flow rate above, the propane mass flow rate should be set at no more than 2.37 g/s, for a total mass flow of 10.4 g/s. The exact orifice diameters used is discussed in **Section 2.3**. It should be noted that this analysis does not account well for loses in the valves and other control elements, and should thus be used only for preliminary sizing. Empirical flow measurements may be needed for refinement and validation.

2.2 Combustion Theory

Next, it is worth considering the principles underlying combustion chamber design. The combustion chamber, as the flaming heart of the rocket, must ensure injection, ignition, and proper mixing of the combustion reagents. Additionally, said reagents must be given sufficient time to combust, lest they be expelled by the nozzle before doing so. While liquid rocket engines must also concern themselves with propellant vaporization, this is not a concern for the gas-fed engine used here. The final design consideration typical of combustion chambers is the avoidance of detonation shocks within [16]. Unfortunately, no simple analytic models exist for that phenomenon, and so this concern is left as an unaddressed risk for testing.

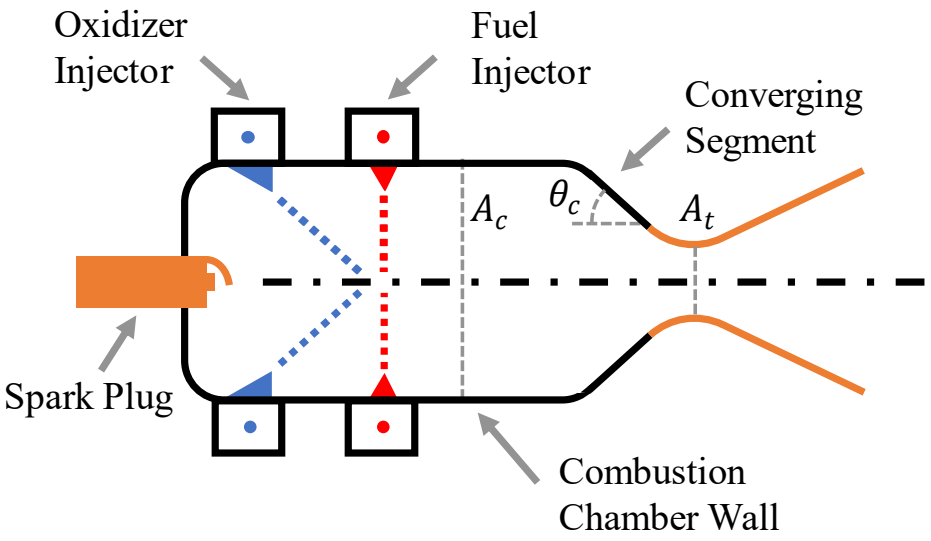

Figure 2.2: Cartoon schematic of a rocket combustion chamber, roughly analogous to the design implemented here. Oxidizer and fuel are injected via impinging jets from circumferential channels, then allowed time to combust, and finally accelerated in the converging segment up until the nozzle throat.

Chamber volume, which can be related to the mean propellant stay time t_s via **Equation 2.3**, is a key parameter for ensuring the combustion reaction has time to complete. Note that V_c is the chamber volume measured between the upstream boundary and the throat plane, and ρ the average gas density.

$$V_c = \frac{\dot{m}_{tot} t_s}{\rho} \tag{2.3}$$

While many geometries exist for combustion chambers, including parabolic, spherical, and near-spherical, offering ideal weight to volume ratios, cylindrical chambers are easier to manufacture, and are thus the type used here. **Figure 2.2** provides a schematic overview of the cylindrical combustion chamber geometry, including a straight converging segment to the throat, as well as the circumferential injectors and an ignition source. Instead of using **Equation 2.3** directly, however, it is common to express the combustion chamber size in terms of the characteristic length, L^*, defined by **Equation 2.4** [16]. This is a more convenient quantity, and can be readily computed from the system geometry. Although determining the appropriate value is difficult to do a priori, published data exists upon which to make an initial selection.

$$L^* = \frac{V_c}{A_t} = \frac{\dot{m}_{tot} t_s}{A_t \rho} \tag{2.4}$$

2.3 Chemical Analysis

A detailed discussion of the chemical analysis needed to predict the mass fractions of the various combustion products and the temperatures developed is beyond the scope of this paper, as it is quite a complex problem. Instead, that analysis was conducted via the Chemical Equilibrium with Applications (CEA) script created by the National Aeronautics and Space Administration [17]. That program uses the principle of minimization of free Gibbs energy, combined with equations of state, to solve for the composition and properties of the exhaust given initial conditions. Included in the script is an extensive database of material properties. The exact parameters provided to that program can be found in **Appendix B**, as well as the results for the sodium-seeded and unseeded fuel mixtures considered. Two results of relevance to the combustion chamber design are that the predicted chamber temperature is $T_c = 3326\,K$, and the throat temperature is $T_t = 3194$.

2.4 Combustion Chamber Design

Combining now the flow parameters of **Section 2.1** with the combustion chamber design principles of **Section 2.2**, along with the global design requirements, the combustion chamber shown in **Figure 2.3** is arrived upon. It uses a cylindrical combustion volume, with a straight angled converging segment leading to the throat. Seven oxygen and five propane circumferential injector holes are used to ensure even flow distribution and mixing, themselves fed via circumferential channels. To ensure to the stochiometric combustion, the oxygen holes are 3/32" (2.38mm) in diameter while the fuel holes are 0.060" (1.52 mm). The oxidizer holes are angled at 45°, creating jets that impinge upon the flow from the fuel holes and thus ensuring better propellant mixture. To ignite the resulting mixture, an NGK CR9EIX commercial spark plug is used, mounted in the extreme upstream position and screwed into the combustion chamber. The CR9EIX was selected due to its high temperature rating. Feeding the injector holes are the flow distributers, also shown in **Figure 2.3**, which are used to spread the single point flow of the input stream into the six injection holes used for each propellant. Grooves are then cut into the distributers to be filled with a sealant paste, such as the BLACK Fiberglass Stove Cement sold on McMaster-Carr, rated to 1090 °C [14]. A cement paste was chosen as no rubber can survive the temperatures experienced,

and copper seals are difficult to package within the volume constraints. Should this prove problematic, a viable but costlier alternative is to instead weld the relevant seams.

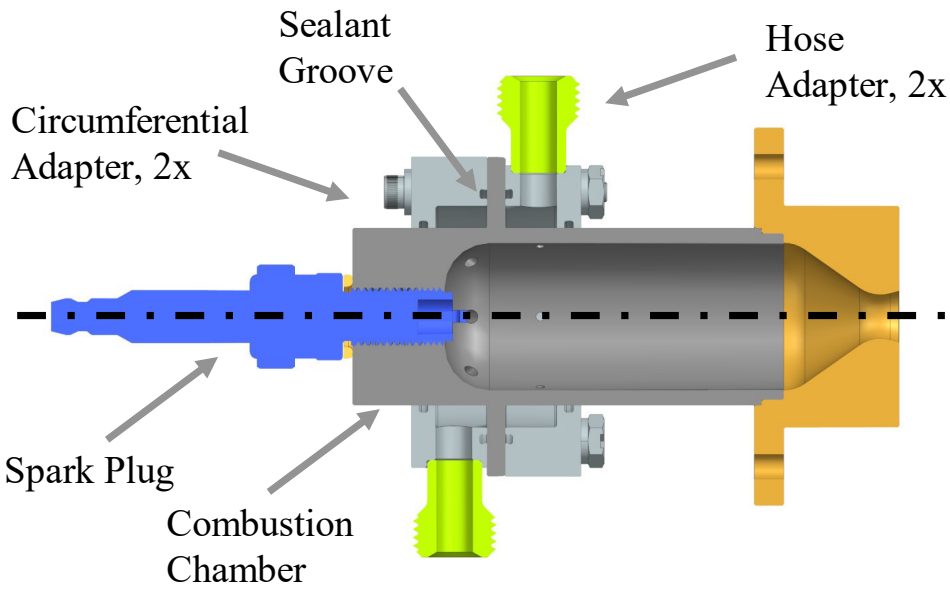

Figure 2.3: Combustion chamber cross-section, orthogonal view.

Next, **Figure 2.4** shows an isometric view of the chamber assembly, including the two hose adapters linking to the circumferential flow distributers. These are pressed and welded into the flow distributers, located on opposing sides of the chamber, and together link the input hoses to the combustion chamber injectors. Each hose adapter has the male fitting for a CGA-022 or 023 fitting, with 5/8”-18 UNF threads [18]. Finally, the circumferential adapters are linked to the thrust chamber piece via a flange with bolt holes, and then fasteners preload the assembly.

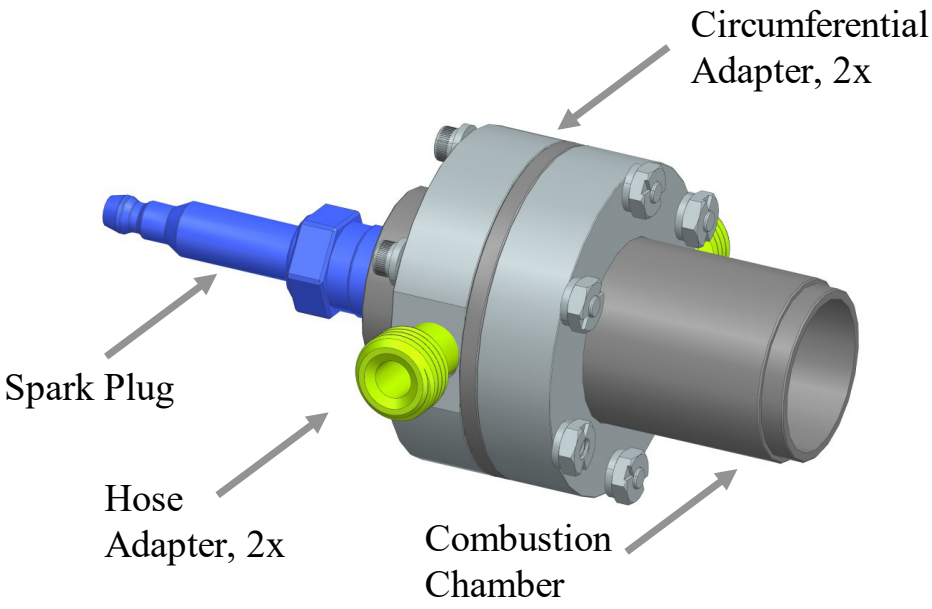

Figure 2.4: An isometric view of the combustion chamber assembly. The hose adapters are shown in green, as indicated, along with the spark plug in blue. Low-grade UNF #6-32 bolts are used to maintain compression on the assembly to ensure proper sealing, with distorted thread nuts used to ensure positive retention at high temperatures.

To determine the dimensions for the design, the required characteristic length L^* had to be determined, as well as the throat diameter. The latter parameter resulted from the analysis in **Section 3.2**, selected to be 0.275in (6.99 mm) in order to match the nozzle total mass flow to that from the feed hoses. Meanwhile, the characteristic length was found from that used by Peterson et al. in their liquid propane engine as at least 500 mm, though they found marginally better performance at 830 mm [19]. A convergence angle was selected at $\theta_c = 35°$, based on typical values used [16]. Using these inputs, as well as **Equation 2.4** and design assembly considerations, the parameters of **Table 2.1** were derived, and form the numeric sizing of the combustion chamber design. The combustion pressure was determined in **Section 2.1**, but is low enough as to create trivial hoop stress in the engine, and is thus not considered further here. Although the temperature in the center of the chamber is extremely high, predicted to be 3326 K, the temperature experienced in the chamber walls is bounded by that in the throat due to the higher convection coefficient (see **Section 3.3**). Thus, the thermal design conducted for the throat in **Section 3.3** is used here as well for material selection and stress margins: the combustion chamber is made of AISI 316 stainless steel to avoid oxidation from the pure oxygen, and passively cooled.

Table 2.1 – Combustion Chamber Parameters	
L_c	50.8 mm (2.00”)
D_c	25.4 mm (1.00”)
D_t	7.62mm (0.300”)
θ_c	45°
L^*	567 mm (22.3”)
P_0	400,000 Pa (58 psi)
T_0	3326 K
$\dot{m}_{O2}$	8.05 g/s
$\dot{m}_{C3H8}$	2.37 g/s
t_s	17.8 ms

3. Flow Acceleration Nozzle

Next, the high temperature flow from the combustion chamber must be accelerated to provide thrust. **Section 3.1** discusses the theory underlying converging-diverging nozzles, also known as de Laval nozzles. **Section 3.2** then discusses the parameters of the de Laval nozzle design for use with this prototype, matching the dimensions of the combustion chamber discussed in **Section 2.4**. Finally, to meet the system requirement for safety and to ensure proper operation, **Section 3.3** uses a thermal network model to analyze the temperatures expected in the throat. It is found that the use of stainless steel throughout the assembly avoids thermal mismatch stress, as well as providing good strength at the needed temperatures, even when passively cooled.

3.1 Nozzle Theory

Since the fundamental purpose of the nozzle is to turn thermal energy into thrust, the total thrust of a nozzle must first be established. Considering the setup of **Figure 3.1**, it can be found that there are two sources of thrust: momentum transfer from the propellant and pressure thrust.

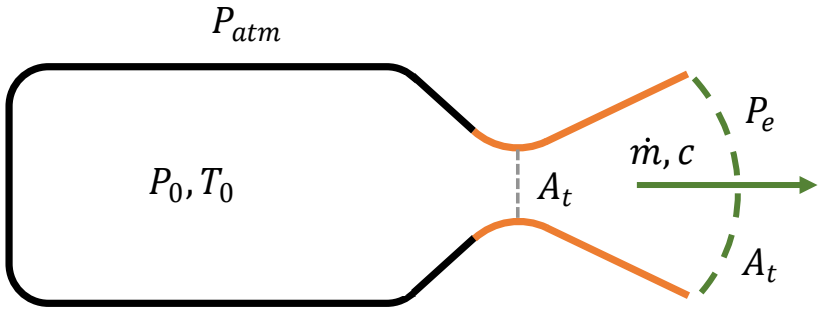

Figure 3.1: Rocket nozzle cross section, schematic. High pressure gas from the combustion chamber is fed into a de Laval nozzle, reaching sonic conditions at the throat, and then expanding to the exhaust pressure P_e on the surface indicated.

Combining the magnitudes of both components, the thrust generated by the rocket can be found via **Equation 3.1**, where P_{atm} is the ambient pressure around the rocket, P_e the exhaust pressure, and A_e the exhaust area.

$$F_{\parallel} = \dot{m}c + (P_e - P_{atm})A_e \tag{3.1}$$

While there is thus some benefit to under-expanded exhaust – namely, the pressure thrust – pressure equilibration occurs via a series of waves and shocks, and has been shown to be less efficient than exactly expanding to ambient, namely $P_e = P_{atm}$ [20]. Although in orbital rockets,

which must transition from sea-level pressure to vacuum, a compromise between expanding to sea level and vacuum is often used, this is not a concern for the prototype developed here, which will operate exclusively in terrestrial pressures.

To analyze the exact nature of the acceleration undergone within the rocket nozzle, several simplifying assumptions are needed, listed below:

a. The combustion creates perfect, homogenous gas, with the properties outputted by the CEA analysis of **Section 2.3**
b. Chemical equilibrium is established in the combustion chamber, and is not changing downstream within the nozzle
c. Adiabatic expansion
d. No friction
e. The gas undergoes one dimensional flow, i.e., to move along parallel streamlines
f. The gas velocity distribution is uniform over each axial cross-section

Given these conditions, it is possible to compute an analytic formula for the exhaust velocity of the nozzle, namely **Equation 3.2**, and thus the thrust, via **Equation 3.1**. The exhaust velocity in **Equation 3.2** depends on the expansion pressure, set equal to P_{atm}, and the gas properties after combustion, namely heat ratio γ_e, combustion temperature T_0, and gas constant R_e [16].

$$c = \sqrt{\frac{2\gamma_e}{\gamma_e - 1} R_e T_0 \left(1 - \left(\frac{P_{atm}}{P_0} \right)^{\frac{\gamma_e - 1}{\gamma_e}} \right)} \tag{3.2}$$

The mass flow rate can also be computed, and is given in **Equation 3.3**, also including the throat area A_t [16]. It is worth noting that this is nothing other than the chocked flow equation for the hot gas in the combustion chamber, discharging via the throat.

$$\dot{m} = P_0 A_t \sqrt{\frac{\gamma_e}{R_e T_0} \left(\frac{2}{\gamma_e + 1} \right)^{\frac{\gamma_e + 1}{\gamma_e - 1}}} \tag{3.3}$$

In order to ensure that the desired expansion to ambient pressure occurs, however, it is necessary to compute the ideal area expansion ratio, $\frac{A_e}{A_t}$. **Equation 3.4** gives the ideal expansion ratio in terms of the exhaust Mach number, M_e and the gas properties [20].

$$\frac{A_e}{A_t} = \frac{1}{M_e} \cdot \left(\frac{2 + (\gamma_e - 1) M_e^2}{\gamma_e + 1} \right)^{\frac{\gamma_e + 1}{2(\gamma_e - 1)}} \tag{3.4}$$

To find M_e, it is necessary to compute the speed of sound in the exhaust, which in turns requires the exhaust temperature. That temperature, T_e, can be readily found by the usual ideal gas adiabatic expansion relation, namely **Equation 3.5** [21].

$$T_e = T_0 \left(\frac{P_{atm}}{P_0} \right)^{\frac{\gamma_e - 1}{\gamma_e}} \tag{3.5}$$

The local speed of sound, a_e, is then computed via **Equation 3.6** [16].

$$a_e = \sqrt{\gamma_e R_e T_e} \tag{3.6}$$

And so the exhaust Mach number is now readily given by **Equation 3.7**.

$$M_e = \frac{c}{a_e} \tag{3.7}$$

Other elements of concern when designing nozzles include the throat radius, shock formation, heating, and various forms of losses. Throat radii between 0.5 to 1.5 times the throat radius are typical, determined empirically [16]. Shocks are difficult to predict, and tend to be minimal in an ideally expanded nozzle, and so no attempt is made to assess their presence. In contrast, thermal analysis to determine component heat capabilities is conducted in **Section 3.3**. Although losses, including thermal losses, affect the total thrust, they need not be pursued further since there is no metric of thrust that must be obtained.

3.2 Nozzle Parameters

Using the formulas above, a nozzle design was arrived upon, as shown in **Figure 3.2**. The throat is a monolithic machined component, and like the combustion chamber, made of AISI 316 stainless steel, threaded on to the combustion chamber via a 1-1/8”-18 thread and located via a separate boss to said combustion chamber. In order to match the mass flow rate determined in **Section 2.2**, namely $\dot{m} = 10.4\, g/s$, the throat diameter was set at 0.300 in (7.62mm), per **Equation 3.3**, and using gas parameters established from **Section 2.3**. Then, to expand the resulting sonic flow, per **Equation 3.4**, the optimum exit diameter was computed at 0.348in

(8.85mm). Additionally, based on empirical rules of thumb, the convergence half-angle was set at 35°, and the divergence half-angle at 15°.

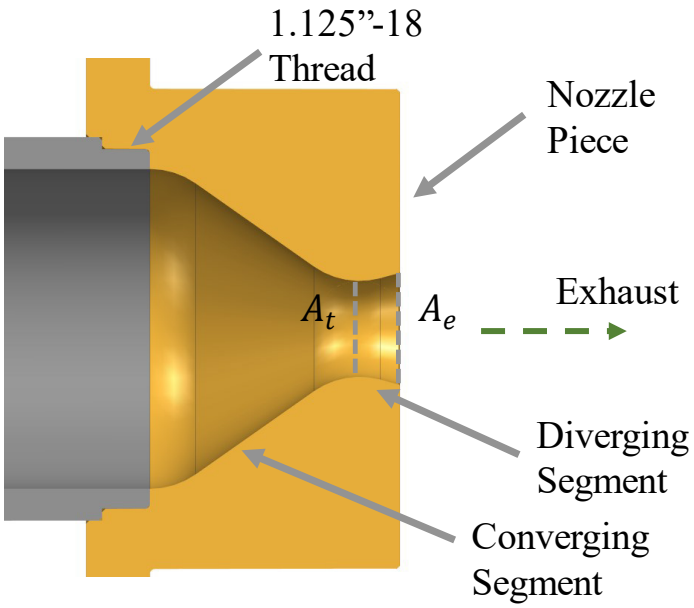

Figure 3.2: The de Laval nozzle design, cross-section. The threaded interface between the combustion chamber and the nozzle piece forms a semi-labyrinth seal, and it is planned to place a sealing cement at the outer seam between them to further enhance the seal.

This creates a nozzle with an exhaust velocity estimated at $c = 1{,}800\ m/s$, per **Equation 3.2**, but an exit Mach number of only $M_e = 1.63$, hence the small expansion needed. Typical rockets have far more energy remaining in the sonic flow in the throat, but here the low chamber pressure results in limited acceleration beyond the throat, and hence the unusually short diverging segment of the nozzle. Given all these parameters, the rocket’s thrust is predicted to be 18.4 N. These nozzle parameters are summarized in **Table 3.1**.

Table 3.1 – Nozzle Design Parameters	
c	1800 m/s
$F_{\parallel}$	18.4 N
M_e	1.63
D_t	7.62 (0.300”)
D_e	8.85 (0.348”)
$P_e = P_{atm}$	101,325 Pa (14.7 psi)

3.3 Nozzle Thermal Analysis

To ensure that the nozzle does not catastrophically melt during operation, it is necessary to evaluate the temperatures it experiences. In turn, within the nozzle, special attention must be paid to the throat, where the convection coefficient is highest, and thus the binding thermal load of the entire assembly is present. The following analysis thus concerns itself with creating a thermal network to model the temperatures present in an axial cross-section at the thrust, as per **Figure 3.3a**. The elements thus indicated in turn are used to form the thermal-network model of **Figure 3.3b**, using the lumped-element assumption to approximate convective and conductive elements as resistors, and the steel heat capacity as a capacitance, as is typical of such models [21].

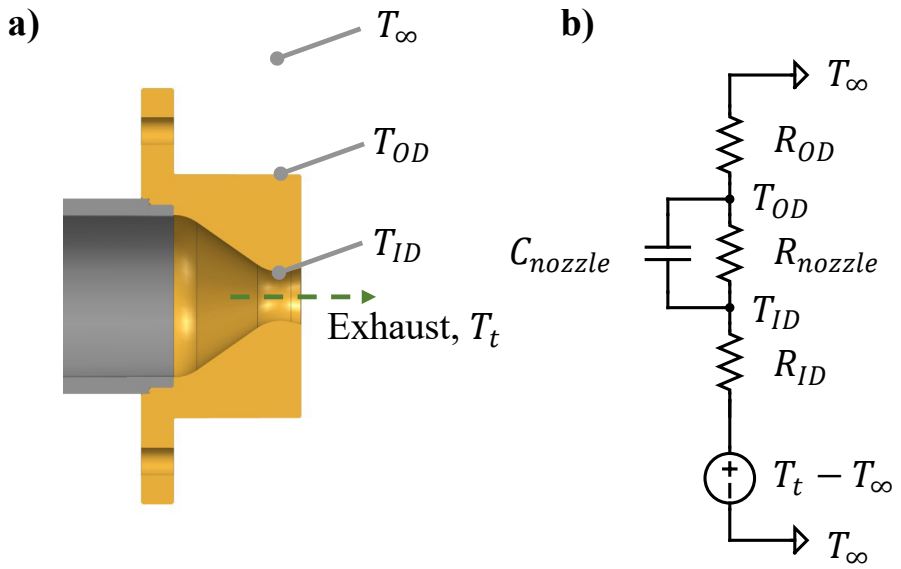

Figure 3.3a: A cartoon schematic cross section of the different components in the thermal system. At the core is the heat reservoir of the combustion plume, radiating heat via convection to the nozzle metal, which is then conducted outward to the surface, and then convected away to the atmosphere via natural convection. **Figure 3.3b**: The thermal network model thus derived, noting that the nozzle metal is a capacitor C_{nozzle} in parallel with a resistor, R_{nozzle}, the inner forced convection with resistance R_{ID}, and the outer free convection as resistor R_{OD}.

It is assumed that the plume and the ambient atmosphere are constant temperature heat reservoirs, of temperatures 3194 K and 300K, respectively. Since this model considers only a single cross-section, all resistance and capacitances are computed per unit length. First, each of the

resistances and capacitances must be computed, and then they will be combined via **Equation 3.8** to find the total resistance, and **Equation 3.9** to find the network time constant.

$$R_{thermal} = R_{ID} + R_{nozzle} + R_{OD} \tag{3.8}$$

$$\tau_{nozzle} = R_{nozzle} \cdot C_{nozzle} \tag{3.9}$$

Considering the nozzle first, it is in some ways simplest. The material properties are assumed constant, and taken from MatWeb data [22]. The capacitance is simply the total nozzle heat capacity, and can thus be found vis **Equation 3.10**, where $D_{t,OD}$ is the nozzle outer diameter, $c_{p,316}$ the specific heat capacity of 316 stainless steel, and ρ_{316} the density of 316 stainless steel. Do note that the steel's material properties are assumed not to vary with temperature.

$$C_{nozzle} = \frac{\pi}{4}\left(D_{t,OD}^2 - D_t^2\right) \cdot \rho_{316} \cdot c_{p,316} \tag{3.10}$$

Likewise, the nozzle resistance can be found from **Equation 3.11**, where k_{316} is the thermal conductivity of 316 stainless steel.

$$R_{nozzle} = \frac{1}{2\pi k_{316}} \ln \frac{D_{t,OD}}{D_t} \tag{3.11}$$

Turning now to the resistance of the plume, it is difficult to attempt an approximation from first principles. Instead, empirical correlations for the convection coefficient have been found over time, such as that published by D. R. Bartz from the Jet Propulsion Laboratory in 1963 [23]. His formula is shown in **Equation 3.12**, in terms of the mass flow rate $\dot{m}$, throat diameter and area D_t and A_t, throat temperature T_t, gas viscosity and specific heat μ_e and $c_{p,e}$. Additionally, it depends heavily on $\bar{T}$, defined in **Equation 3.13**, which is the average of the throat surface temperature and the temperature at the core of the plume, reflecting the averaging of the material properties in Bartz's analysis.

$$h_{ID} = \frac{0.026}{D_t^{0.2}} \left(\frac{\dot{m}}{A_t}\right)^{0.8} \mu_e c_{p,e} \left(\frac{T_t}{\bar{T}}\right)^{0.68} \tag{3.12}$$

$$\bar{T} = \frac{T_t + T_{ID}}{2} \tag{3.13}$$

Note the inverse dependence on the diameter in **Equation 3.12**, justifying the use of the minimum nozzle diameter as the bounding thermal case. In order to use **Equation 3.12**, the

material properties at $\bar{T}$ must be determined, as well as the temperature $\bar{T}$ itself. $c_{p,e}$ is taken from the CEA analysis of **Section 2.3**, and assumed to not vary strongly with temperature. μ_e, however, is not available from the CEA computations, and is thus computed as the mass average of the room temperature viscosities of the combustion products, and then adjusted for temperature via the relationship in **Equation 3.14** [23].

$$\mu(T) = \mu_{ref}\left(\frac{T}{T_{ref}}\right)^{0.6} \tag{3.14}$$

Meanwhile, while at first appraisal, the use of $\bar{T}$ in **Equation 3.12** may seem circular – h_{ID} depends on $\bar{T}$, T_{ID} depends on h_{ID}, and yet $\bar{T}$ is itself a function of T_{ID} – this can be readily solved via iteration between an initial guess for $\bar{T}$ and that computed from the thermal network resulting. This process converges rapidly, although no detailed study of that convergence was conducted for this project. The convection coefficient can then be readily converted into the convective resistance via **Equation 3.15**.

$$R_{ID} = \frac{1}{h_{ID}\pi D_t} \tag{3.15}$$

Finally, as with Brantz's formula for the engine thrust plume convection, an empirical correlation must be used to find the natural convection rate from the outer surface of the nozzle. **Equation 3.16** provides an estimation of the Nusselt number, Nu, of a horizontally mounted cylinder, where the Nusselt number is in turn related to the natural convection coefficient via **Equation 3.17** [24].

$$Nu = 0.36 + \frac{0.518 \cdot Ra^{0.25}}{\left(1 + \left(\frac{0.559}{Pr}\right)^{9/16}\right)^{4/9}} \tag{3.16}$$

$$Nu = \frac{h_{OD}k_{316}}{D_{t,o}} \tag{3.17}$$

However, **Equation 3.16** is written in terms of the Rayleigh number and the Prandtl number, which must themselves be computed. The Prandtl number can be found directly via **Equation 3.18**, once the gas properties are known. The Rayleigh number is more complicated;

Equation 3.19 relates it to the Grashof number, Gr, and the Prandtl number Pr, where the former is in turn defined in **Equation 3.20**.

$$Pr = \frac{\mu_{air} c_{p,air}}{k_{air}} \tag{3.18}$$

$$Ra = Pr \cdot Gr \tag{3.19}$$

$$Gr = \frac{g \rho_{air}^2 (T_f - T_\infty) D_{t,OD}^3}{T_f \mu_{air}^2} \tag{3.20}$$

Note the use of an intermediate film temperature T_f, defined in **Equation 3.21**. This represents an averaging of the gas properties between the surface temperature of the nozzle and the ambient temperature, and is used both directly in **Equation 3.19**, and in the computation of the gas properties.

$$T_f = \frac{T_{OD} + T_\infty}{2} \tag{3.21}$$

Since the above method for determining h_{OD} is itself a function of the nozzle surface temperature, T_{OD}, as with **Equation 3.12**, iteration must be used to converge to a value, updating both the gas properties of air from reference tables and the Grashof number. Indeed, iteration must be used to simultaneously solve for both T_{OD} and T_{ID}, but this is still readily possible.

Combining these resistances and capacitors, per the model in **Figure 3b**, the total equivalent resistance per unit length is given by $R_{thermal} = 4.86 \frac{K}{Wm}$. The individual resistances, and the resulting steady-state temperatures at each interface, are summarized in **Table 3.2.** As is required for safe operation, the steady-state nozzle temperature is 620 C, well below the melting point at 1370 C [22]. Furthermore, the time constant is large at $\tau_{nozzle} = 27\ s$ per **Equation 3.9**, indicating that for firings under half a minute, the temperature rise in the throat will be less than 63% of the steady-state values indicated in **Table 3.2**. The use of AISI 316 stainless steel throughout the rocket design thus ensures it is capable to the temperatures needed for reasonable firings length, meeting the requirements for both design safety and safety to the user from potential thermal failures.

Table 3.2 – Nozzle Thermal Parameters	
R_{ID}	3.86 K/Wm
R_{nozzle}	0.0068 K/Wm

C_{nozzle}	3.97 kJ/Km
R_{OD}	0.99 K/Wm
$R_{thermal}$	4.86 K/Wm
τ_{nozzle}	27 s
T_{ID}	620 C
T_{OD}	616 C

4. Magnetic Plume Steerage

With the basic infrastructure of a rocket engine now designed, the next step is to create the magnetic steering mechanism for the plume. **Section 4.1** thus analyzes the ionic content of the plume, in order to determine the magnitude of magnetic force that can be created, proportional to the magnetic field. **Section 4.2** then implements a magnetic circuit to generate the needed magnetic field, allowing for the steering of the thrust plume when said circuit is activated.

4.1 Steering Force Analysis

Unfortunately, due to the complex nature of the highly collisional plasmas, such as the rocket thrust plume, the following calculation shall be of low fidelity. Despite the ionic nature of the components, the hard sphere collision theory is assumed to simplify the calculations. **Equation 4.1** permits the computation of the collision frequency ν_{AB} between species A and B, in terms of their masses m_A and m_B, collision radii r_A and r_B, Boltzmann constant k_B, and species number densities N_A and N_B [25].

$$\nu_{A,B} = N_A N_B \pi (r_A + r_B)^2 \sqrt{8\pi k_B T \cdot \frac{m_A + m_B}{m_A m_B}} \tag{4.1}$$

While the individually ionized species will differ, to a coarse approximation, the initial number density of electrons N_e will be approximately equal to the initial number density of cations N_+, that is, $N_{e^-} \approx N_+$. Simplifying the computation to consider only the neutral carbon dioxide (CO_2), which forms the plurality of the exhaust mass at 27%, the relative collision rates of electrons vs the most common cation, hydronium (H_3O^+), is shown in **Equation 4.2**. Note that species cross sectional radii are taken from sums of atomic radii, and are loose estimates.

$$\frac{\nu_{H_3O^+,CO_2}}{\nu_{e^-,CO_2}} = \frac{N_{H_3O^+}}{N_{e^-}} \cdot \frac{\left(r_{CO_2} + r_{H_3O^+}\right)^2}{\left(r_{CO_2} + r_{e^-}\right)^2} \cdot \sqrt{\frac{m_{e^-}}{m_{H_3O^+}} \frac{m_{CO_2} + m_{H_3O^+}}{m_{CO_2} + m_{e^-}}} \approx 10^{-2} \tag{4.2}$$

Although the collision rate of the electrons is thus 10^2 times faster than the ions, the electrons themselves weigh only 0.003% of the cations, and will thus, by Newton's second law, be accelerated by the Lorentz force (which is proportional only to the charge, not the mass), 34,000 times faster than the ions. Even accounting for the collisions, it is still likely that the electrons will

escape the magnetic field entirely, and thus leave only the cations to impart momentum on the uncharged gas.

Next, to assess the magnitude of charge present for that momentum transfer, it is necessary to evaluate the ionic content of the plume, sourced from both chemical and thermal ionizations. The Saha equation, presented in **Equation 4.3**, provides a coarse estimation of the ionization fraction of a plasma in thermal equilibrium [26]. Note that n_e and n_i are the number densities of the electrons and ions, respectively, n_o the neutral number density, h Planck's constant, m_e an electron's mass, and χ_i the ionization energy of the ionization under consideration.

$$\frac{n_e n_i}{n_o} = 2\frac{(2\pi m_e k_B T)^{3/2}}{h^3} \cdot e^{-\frac{\chi_i}{k_B T}} \tag{4.3}$$

Equation 4.3 is intended for use in high temperature, low-collisionality homogeneous plasmas; the rocket plume is high pressure, low temperature (by the standards of plasmas), and fundamentally heterogenous in composition. It is thus merely a coarse estimate, but as shall be shown, easily demonstrates an order of magnitude difference between the thermal ionization concentration and the intermediate chemical species. Since the thermal ionization fraction depends exponentially on the temperature and the ionization energy χ_i, only H_2 will experience meaningful ionization at 3300 K. The hydrogen ionization thus results in a charge concentration per gram of exhaust of $\rho_{thermal} = 1.49 \cdot 10^{-7}\ C/g$.

In contrast, **Table 4.1** shows the ionized species concentrations estimated in **Section 2.3**. The total pseudo-current I^* can then be computed via **Equation 4.4**, where $\rho_{chemical}$ is the mass fraction of ionized species, and $\rho_{thermal}$ is the mass fraction from chemical sources, i.e., from **Table 4.2**.

$$I^* = \dot{m} \cdot (\rho_{chemical} + \rho_{thermal}) \tag{4.4}$$

Table 4.1 – CEA Ionized Species Concentrations

Species	Unseeded Mass Fraction	Seeded Mass Fraction
H_3O^+	9.60E-09	N/A
OH^-	9.01E-10	1.83E-06
HCO^+	3.05E-10	N/A
O^-	2.52E-10	5.14E-07

O_2^+	1.59E-10	N/A
H_2O^+	1.13E-10	N/A
O_2^-	8.84E-11	1.82E-07
Na^+	N/A	2.46E-05
H^-	N/A	1.86E-09
HO_2^-	N/A	6.87E-10
Na^-	N/A	4.05E-10
$NaOH^-$	N/A	8.18E-11
Na_2O^+	N/A	5.62E-11

Computing $\rho_{chemical}$, it is found to be $4.4 \cdot 10^{-5} C/g$ when unseeded by sodium. The force can now be found from **Equation 1.3**, re-written in terms of the pseudo-current I^* in **Equation 4.5**.

$$F_\perp = I^* \cdot B \tag{4.5}$$

In **Section 4.2**, it is found that a field strength of 710 mT is achievable, and hence for the unseeded case, a perpendicular force of $F_\perp = 0.3\ mN$ is created. This is, unfortunately, so small as to be non-existent relative to $F_\parallel$. Previous studies on rocket thrust plume plasma properties have found, however, a strong dependence between the ionization and the alkaline metal concentration [27]. If instead a small quantity of an alkaline metal is added, such as sodium, a far greater number of ions form in the plume. When 0.5% sodium by mass is added, the ion density rises to $\rho'_{chemical} = 8.9 \cdot 10^{-2} C/g$, and so the Lorentz force increases to $F'_\perp = 0.65\ N$, equal to 3.5% of the total engine thrust, a far more useful quantity, meeting the requirement for at least 1% thrust deflection. It is thus recommended that if Lorentz steering is to be used, alkaline seeding by implemented. Little characterization was done of the effect of increasing alkaline concentration, nor on the alkaline selection; further work will be needed here for a practical selection to be made. At initial inspection, sodium carbonate, Na_2CO_3, is a promising candidate for its wide availability, non-volatility, and lack of toxicity. Furthermore, a precise mechanism will need to be designed to appropriately seed the plume; such was not implemented here.

4.2 Magnetic Circuit Design

Finally, a magnetic circuit must be created to generate the needed magnetic field. In order to produce a high magnetic field via electromagnetic solenoids requires either a great amount of windings, and hence copper, or a high current, resulting in large resistive losses. An alternative is the use of a magnetizable material, which will guide the magnetic flux as well as amplifying it. Such a circuit can be seen in **Figure 4.1**, linking the throat of the rocket engine to an externally mounted solenoid. Said solenoid is quite large, trading increased copper requirements for a lower total current. By running 40 A through that coil, a magnetic flux density of 64 mT is created. This flux is then concentrated within the throat via the flux concentrators, as indicated, each with the same diameter as the throat, decreasing the total area relative to the core and thus increasing the flux density due to the conservation of that flux.

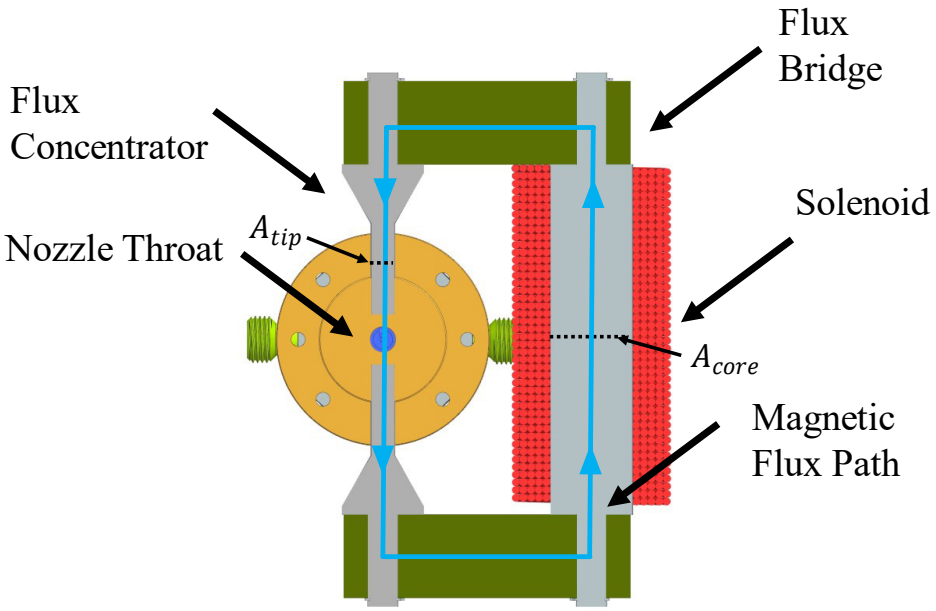

Figure 4.1: Cross section of the magnetic steering circuit, taken at the throat of the engine. Note the coil is wrapped five times around a core of diameter 25.4 mm (1”), with the flux then transmitted to the throat via the flux bridges and concentrators. The wires used are of gauge 12, and enameled to provide insulation.

In order to find a suitably high magnetic permeability material to guide the flux, a non-austenitic steel was selected, specifically AISI 416 stainless steel. Chosen for the same reasons of corrosion resistance as the stainless in the nozzle and to match the thermal expansion characteristics of AISI 316 stainless, this material has a permeability estimated at μ_{416}~$700\mu_0$,

where μ_0 is the permeability of vacuum [28]. Hopkinson's law, given in **Equation 4.6,** can then be used to numerically estimate the magnetic flux in a closed magnetic circuit [13]. That law states that the magnetomotive force, $\mathcal{F}_{MMF}$, is equal to the product of the reluctance $\mathcal{R}_{eq}$ and the total magnetic flux Φ_B, akin to Ohm's law for electrical circuits.

$$\mathcal{F}_{MMF} = \Phi_B \mathcal{R} \tag{4.6}$$

Continuing the circuit analogy, a circuit model of the flux linkages can be found in **Figure 4.2**. Forming a simple series circuit with resistors and a voltage source, the total resistance is readily found from **Equation 4.7**, where $\mathcal{R}_{gap}$ is the reluctance across the gap between the concentrators, and $\mathcal{R}_{core}$ the reluctance through the 416 flux linkages.

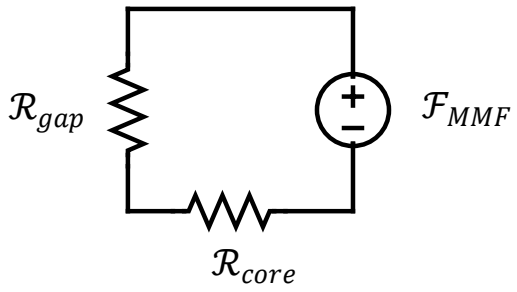

Figure 4.2: Circuit model of the magnetic circuit shown in **Figure 4.1**, used to create a high magnetic field in the nozzle throat. $\mathcal{F}_{MMF}$ is the magnetomotive force due to the coil, $\mathcal{R}_{gap}$ the reluctance of the gap between the concentrators, and $\mathcal{R}_{core}$ the reluctance of the flux core.

$$\mathcal{R}_{mag} = \mathcal{R}_{gap} + \mathcal{R}_{core} \tag{4.7}$$

To calculate $\mathcal{R}_{gap}$, it is assumed that the AISI 316 stainless steel used in the nozzle has the same permeability as vacuum. If this is not the case, it may very well deflect the magnetic field away from the throat; such could happen do to cold working due to machining, and so the magnetic field should be tested before ignition to ensure this has not occurred. Then, with that assumption, the gap reluctance is found via **Equation 4.8,** and the core reluctance similarly through **Equation 4.9**.

$$\mathcal{R}_{gap} = \frac{\ell_{gap}}{\mu_0 A_{tip}} \tag{4.8}$$

$$\mathcal{R}_{core} = \frac{\ell_{core}}{\mu_{416} A_{core}} \tag{4.9}$$

The magnetomotive force can now be found from **Equation 4.10**, and then combined into **Equation 4.6**, noting $\Phi_B = AB$ everywhere within the circuit, the magnetic flux density in the gap can be determined. N_{coil} is the number of turns in the solenoid, and I_{coil} the current through those turns.

$$\mathcal{F}_{MMF} = N_{coil} I_{coil} \tag{4.10}$$

Targeting a magnetic flux density of at least 0.5 T within the gap, the coils and concentrators are sized so as to achieve 0.71 T, with the other parameters as listed. Then, to ensure that the coils do not melt, similar to the concerns of **Section 3.3**, the Joule dissipation through the coil is computed to be 142 W. Assuming no heat leakage due to convection, and modeling the coil as a single lumped mass, the temperature in the coils increases at a rate of 0.7 K/s, easily allowing for a half minute firing time before reaching a dangerous temperature. Unfortunately, to increase the magnetic field further requires both careful optimization of the coil resistances versus magnetic field strength, and selection of a higher magnetic saturation core material, design exercises which are not pursued here. Several key parameters of the magnetic circuit and the attached coil are now given in **Table 4.2**, forming the last component of the design, creating the magnetic flux density that will in turn apply a Lorentz force to the thrust plume, steering it as desired. Note that as $\mathcal{R}_{gap} \gg \mathcal{R}_{core}$, the uncertainty in the permeability of the AISI 416 stainless steel is of low importance.

Table 4.2 – Magnetic Circuit Parameters

B_{gap}	62 mT
B_{core}	710 mT
I_{coil}	40 A
$\mathcal{R}_{gap}$	260,000,000 1/H
$\mathcal{R}_{core}$	898,000 1/H
$\dot{T}_{coil}$	0.7 K/s
R_{coil}	88.61 mΩ
P_{coil}	142 W
λ_{coil}	7.04 mH

N_{coil}	217
ℓ_{gap}	15.24 mm (0.600”)

5. Conclusion

Beginning from a prime consideration of safety, the feed system to a rocket engine was designed, and then a stainless-steel combustion chamber sized to match. Next, a de Laval nozzle was attached to the combustion chamber to expand the flow, accelerating it to an exhaust velocity of 1800 m/s and a thrust of 18.4 N. The thermal conditions within that nozzle were analyzed via a thermal network model and Bartz’s formula, such that the steady state temperature was found not to exceed 621 C, with a time constant of 27 s. Finally, a magnetic circuit was attached around the nozzle, creating a magnetic flux density within the throat of 710 mT. Without alkaline seeding, the perpendicular thrust created is estimated at 0.6 mN. With a small amount of added sodium, however, a perpendicular thrust component up to 3.5% of the total thrust is expected, permitting reasonable steering of a vehicle’s trajectory. As shall be described in detail in **Section 5.1**, a prototype must be constructed to validate the assumptions used both for the design and in the prediction of the plume steerage. Nevertheless, this initial analysis shows promise as an alternative thrust vector control technique, avoiding heavy actuated mechanisms in favor of a solid-state magnetic coil.

5.1 Future Work

In order to complete the design discussed in the foregoing pages, several key elements remain. The electronic control circuitry must be designed in its entirety, and components selected for the gas supply system. A mounting structure for the rocket should be created, and instrumentation devised to apply thereto in order to measure both the axial and perpendicular thrust created. It is further recommended that thermistors be added at several points to monitor temperatures, and a Digital Schlieren Imaging suite added to view the effect of the magnetic steering upon the thrust plume gas dynamics.

Then, after manufacturing and assembly are complete, validation and testing should commence. Key design parameters to be checked before firing include the assumptions of flow rates from the input lines through the injectors, integrity of the gaskets and seals, and the

magnetic field strength generated in the throat. Then, hot firings will likely reveal further lessons regarding the combustion chamber and nozzle design that may necessitate design parameter refinement. With the engine then operational, characterization of the effect of the magnetic field upon the plume can commence, evaluating the numeric predictions of this paper.

6. Bibliography

[1] Daniel Klepper and Robert Kolenkow, 2014, *An Introduction to Mechanics*, Cambridge University Press.

[2] George P. Sutton and Oscar Bilbarz, 2010, *Rocket Propulsion Elements*, Wiley.

[3] Sutton, G. P., 2003, "History of Liquid Propellant Rocket Engines in the United States," Journal of Propulsion and Power, **19**(6), pp. 978–1007.

[4] Robert Davies, 1968, *A Study of Saturn V And Intermediate Vehicle Improvement Programs Executive Summary Report*, NASA TM X-53723, National Aeronautics and Space Administration.

[5] Deere, K. A., 2003, "Summary of Fluidic Thrust Vectoring Research Conducted at NASA Langley Research Center," Orlando, FL.

[6] Maruyama, Y., Sakata, M., and Takahashi, Y., 2019, "Performance Analyses of Fluidic Thrust Vector Control System Using Dual Throat Nozzle," *AIAA Propulsion and Energy 2019 Forum*, American Institute of Aeronautics and Astronautics, Indianapolis, IN.

[7] Wu, K., Kim, H. D., and Jin, Y., 2019, "Fluidic Thrust Vector Control Based on Counter-Flow Concept," Proceedings of the Institution of Mechanical Engineers, Part G: Journal of Aerospace Engineering, **233**(4), pp. 1412–1422.

[8] Lee, E., Kang, H., and Kwon, S., 2019, "Demonstration of Thrust Vector Control by Hydrogen Peroxide Injection in Hybrid Rockets," Journal of Propulsion and Power, **35**(1), pp. 109–114.

[9] Zmijanovic, V., Lago, V., Sellam, M., and Chpoun, A., 2014, "Thrust Shock Vector Control of an Axisymmetric Conical Supersonic Nozzle via Secondary Transverse Gas Injection," Shock Waves, **24**(1), pp. 97–111.

[10] Fearn, D. G., 2001, "Ion Thruster Thrust Vectoring Requirements and Techniques," *27th IEPC*, Pasadena, CA.

[11] Masafumi Edamoto, Taichi Morita, Yuki Nishioka, and Naoji Yamamoto, 2019, "Experimental Demonstration of Thrust Vectoring Magnetic Nozzle with Multi-Axis Thrust Measurement System," *37th IEPC*, Vienna, Austria.

[12] Chao Huo, 2021, "Magnetically Controlled Thrust Vector Control Device for Solid Rocket Engine," China, CN202110680367A.

[13] James R. Melcher and Herbet H. Woodson, 1968, *Electromechanical Dynamics*, John Wileys & Sons, Inc.

[14] "McMaster-Carr" [Online]. Available: https://www.mcmaster.com/. [Accessed: 02-Nov-2022].

[15] Frank M. White, 2011, *Fluid Mechanics*, McGraw-Hill.

[16] Dieter K. Huzel and David H. Huang, 1967, *Design of Liquid Propellant Rocket Engines*, National Aeronautics and Space Administration.

[17] Sanford Gordon and Bonnie J. McBride, 1994, *Computer Program for Calculation of Complex Chemical Equilibrium Compositions and Applications*, NASA Reference Publication 1311, National Aeronautics and Space Administration.

[18] "CONCOA CGA Connection Reference Chart" [Online]. Available: https://www.concoa.com/cgachart.html. [Accessed: 08-Jan-2023].

[19] Donald A. Peterson, Jerry M. Winter, and Albert J. Pauli, 1969, *Design, Development, and Testing of a 1,000 Pound (4,450 N) Thrust FLOX-Propane Ablative Rocket Engine*, NASA TM X-1837, National Aeronautics and Space Administration.

[20] Pasquale M. Sforza, 2012, *Theory of Aerospace Propulsion*, Elsevier Science & Technology.
[21] Cravalho, E., Smith, J., Brisson, J., and McKinley, G., 2005, *Thermal Fluids Engineering, An Integrated Approach to Thermodynamics, Heat Transfer, and Fluid Mechanics*, Oxford University Press.
[22] "316 Stainless Steel, Annealed Bar" [Online]. Available: https://www.matweb.com/search/DataSheet.aspx?MatGUID=dfced4f11d63459e8ef8733d1c7c1ad2. [Accessed: 09-Jan-2023].
[23] D. R. Bartz, 1963, *TURBULENT BOUNDARY-LAYER HEAT TRANSFER FROM RAPIDLY ACCELERATING FLOW OF ROCKET COMBUSTION GASES AND OF HEATED AIR*, N65-23286, Jet Propulsion Laboratory.
[24] Anthony F. Mills, 1995, *Heat and Mass Transfer*, CRC Press.
[25] Peter Atkins and Julio De Paula, 2006, *Physical Chemistry For The Life Sciences*, W. H. Freeman and Company.
[26] Karl-Heinz Spatschek, 2012, *High Temperature Plasmas, Theory, and Mathematical Tools for Laser and Fusion Plasmas*, WILEY-VCH Verlag GmbH & Co.
[27] Richard H. C. Lee, I-Shih Chang, and Gordon E. Stewart, 1982, *Studies of Plasma Properties in Rocket Thrust Plumes*, SD-TR-82-44, Space Division Air Force Systems Command.
[28] "416 Stainless Steel" [Online]. Available: https://matweb.com/search/datasheet.aspx?matguid=87084f2733d84828a72052812ac4311b&n=1&ckck=1. [Accessed: 10-Jan-2023].

Appendix

A. Variable Names

A_c: Combustion chamber cross sectional area

A_{core}: Magnetic core cross sectional area

A_e: Nozzle exit cross sectional area

a_e: Local speed of sound in exhaust at nozzle exit

A_{hose}: Cross sectional area of feed hose

A_t: Nozzle throat cross sectional area

A_{tip}: Magnetic circuit concentrator tip cross sectional area

B: Magnetic flux density

B_{gap}: Magnetic flux density in gap between concentrators

B_{core}: Magnetic flux density in circuit core

c: Rocket engine exhaust velocity

C_D: Discharge coefficient

C_{nozzle}: Nozzle thermal capacitance per unit length

$c_{p,316}$: Specific heat capacity of AISI 316

$c_{p,air}$: Specific heat capacity of air

$c_{p,e}$: Specific heat capacity of engine exhaust gases at exit

D_c: Combustion chamber diameter

D_t: Throat diameter

$D_{t,o}$: Throat component outer diameter

D_e: Nozzle exit diameter

$F_\perp$: Perpendicular thrust generated

$F_\parallel$: Parallel thrust generated

$\mathcal{F}_{MMF}$: Magnetomotive force

g: Gravitational acceleration on Earth

Gr: Grashof number

h: Planck's constant

h_{ID}: Convection coefficient within inner diameter of nozzle throat

h_{OD}: Convection coefficient on outer diameter of nozzle throat

I^*: Pseudo-current magnitude present in exhaust

I_{coil}: Current through solenoid coils

I_{sp}: Specific impulse

J: Current density

k_{316}: Thermal conductivity of AISI 316

k_{air}: Thermal conductivity of air

k_B: Boltzmann's constant

L^*: Combustion chamber characteristic length

ℓ_{gap}: Gap length between flux concentrators

ℓ_{core}: Total length of magnetic core

m_0: Rocket initial mass

m_A: Mass of species A

m_B: Mass of species B

M_e: Mach number at nozzle exit

m_e: Mass of an electron

m_f: Rocket final mass

$\dot{m}$: Mass flow rate through nozzle throat

$\dot{m}_{hose}$: Mass flow rate through feed hose

$\dot{m}_{tot}$: Total mass flow rate through feed system

$\dot{m}_{O_2}$: Mass flow rate of O_2

$\dot{m}_{C_3H_8}$: Mass flow rate of C_3H_8

N_+: Number density of cations

N_A: Number density of species A

N_B: Number density of species B

N_{coil}: Number of turns in solenoid

N_e: Number density of electrons

n_e: Number density of electrons due to thermal ionization

n_i: Number density of ions due to thermal ionization

n_o: Number density of neutral species pre-ionization

Nu: Nusselt number

P_0: Combustion chamber pressure

P_{atm}: Atmospheric pressure

P_{coil}: Power dissipation in solenoid

P_e: Pressure at nozzle exit

P_{in}: Input pressure in feed lines

Pr: Prandtl number

R: Specific gas constant

R_e: Gas constant of exhaust gas

R_{ID}: Thermal resistance of nozzle inner diameter to plume

R_{nozzle}: Thermal resistance of nozzle between inner and outer diameters

R_{OD}: Thermal resistance of nozzle between outer diameter and ambient

$R_{thermal}$: Equivalent total thermal resistance

Ra: Rayleigh number

r_A: Collision radius of species A

r_B: Collision radius of species B

r_{CO_2}: Collision radius of CO_2

r_{e^-}: Collision radius of an electron

$r_{H_3O^+}$: Collision radius of H_3O^+

$\mathcal{R}$: Magnetic reluctance

$\mathcal{R}_{core}$: Reluctance of magnetic core

$\mathcal{R}_{gap}$: Reluctance of gap

T_0: Combustion temperature

T_e: Temperature of exhaust at nozzle exit

T_f: Film temperature

T_{ID}: Temperature of throat inner diameter

T_{in}: Temperature of gas at input

T_∞: Ambient temperature

T_{OD}: Temperature of nozzle outer diameter

T_{ref}: Reference temperature

$\bar{T}$: Average of nozzle inner diameter and plume temperatures

t_s: Mean stay time of propellant in the combustion chamber

$\dot{T}_{coil}$: Rate of temperature increase in solenoid during operation

V_c: Combustion chamber volume

Δv: Change in velocity

γ: Ratio of gas specific heat capacities

γ_e: Specific heat ratio of exhaust gas

λ_{coil}: Solenoid inductance

Φ_B: Magnetic flux

θ_c: Nozzle convergence angle

θ_d: Nozzle divergence angle

ρ: Density

ρ_{316}: Density of AISI 316

ρ_{air}: Density of air

$\rho_{chemical}$: Charge density due to chemical ionization

$\rho_{thermal}$: Charge density due to thermal ionization

τ_{nozzle}: Nozzle thermal time constant

μ_{316}: Magnetic permeability of AISI 316

μ_{416}: Magnetic permeability of AISI 416

μ_{air}: Dynamic viscosity of air

μ_e: Dynamic viscosity of exhaust gas

μ_{ref}: Reference dynamic viscosity

$\nu_{A,B}$: Collision frequency between species A and B

$\nu_{H_3O^+,CO_2}$: Collision frequency between H_3O^+ and CO_2

ν_{e^-,CO_2}: Collision frequency between e^- and CO_2

χ_i: Ionization energy of species i

B. CEA Script

Unseeded Input File:

```
### CEA analysis performed on Tue 10-Jan-2023 06:35:59

# Problem Type: "Rocket" (Finite Area Combustor)

prob case=_____2004 ro equilibrium  ions  fac

!Mass Flux/Chamber Area, kg/sec-sqm:
mdot=20.23

# Pressure (1 value):
p,psia= 58
```

```
# Oxidizer/Fuel Wt. ratio (1 value):
o/f= 3.64

# You selected the following fuels and oxidizers:
reac
fuel C3H8            wt%=100.0000
oxid O2              wt%=100.0000

# You selected these options for output:
# short version of output
output short
# Proportions of any products will be expressed as Mass Fractions.
output massf
# Heat will be expressed as siunits
output siunits
# Trace variable:
output trace=1e-10

# Input prepared by this script:/var/www/sites/cearun.grc.nasa.gov/cgi-bin/CEARUN/prepareInputFile.cgi

### IMPORTANT:  The following line is the end of your CEA input file!
end
```

Unseeded Output File:

```
      NASA-GLENN CHEMICAL EQUILIBRIUM PROGRAM CEA2, FEBRUARY 5, 2004
            BY  BONNIE MCBRIDE AND SANFORD GORDON
      REFS: NASA RP-1311, PART I, 1994 AND NASA RP-1311, PART II, 1996

 ***************************************************************************


 ### CEA analysis performed on Tue 10-Jan-2023 06:35:59

 # Problem Type: "Rocket" (Finite Area Combustor)
```

prob case=_____2004 ro equilibrium ions fac

!Mass Flux/Chamber Area, kg/sec-sqm:
mdot=20.23

Pressure (1 value):
p,psia= 58

Oxidizer/Fuel Wt. ratio (1 value):
o/f= 3.64

You selected the following fuels and oxidizers:
reac
fuel C3H8 wt%=100.0000
oxid O2 wt%=100.0000

You selected these options for output:
short version of output
output short
Proportions of any products will be expressed as Mass Fractions.
output massf
Heat will be expressed as siunits
output siunits
Trace variable:
output trace=1e-10

Input prepared by this script:/var/www/sites/cearun.grc.nasa.gov/cgi-bin/CEARU
N/prepareInputFile.cgi

IMPORTANT: The following line is the end of your CEA input file!
end

THEORETICAL ROCKET PERFORMANCE ASSUMING EQUILIBRIUM

COMPOSITION DURING EXPANSION FROM FINITE AREA COMBUSTOR

Pin = 58.0 PSIA

MDOT/Ac = 20.230 (KG/S)/M**2 Pinj/Pinf = 1.001555

CASE = _____

REACTANT		WT FRACTION (SEE NOTE)	ENERGY KJ/KG-MOL	TEMP K
FUEL	C3H8	1.0000000	0.000	0.000
OXIDANT	O2	1.0000000	0.000	0.000

O/F= 3.64000 %FUEL= 21.551724 R,EQ.RATIO= 0.996797 PHI,EQ.RATIO= 0.996797

	INJECTOR	COMB END	THROAT
Pinj/P	1.0000	1.0031	1.7215
P, BAR	3.9989	3.9865	2.3230
T, K	3321.11	3320.49	3189.84
RHO, KG/CU M	3.3048-1	3.2952-1	2.0313-1
H, KJ/KG	0.00064	-1.8836	-637.12
U, KJ/KG	-1210.05	-1211.68	-1780.70
G, KJ/KG	-40916.5	-40912.7	-39938.1
S, KJ/(KG)(K)	12.3201	12.3207	12.3207
M, (1/n)	22.820	22.821	23.192
(dLV/dLP)t	-1.07248	-1.07248	-1.06871
(dLV/dLT)p	2.3580	2.3582	2.3442
Cp, KJ/(KG)(K)	11.3542	11.3570	11.5047
GAMMAs	1.1185	1.1185	1.1143
SON VEL,M/SEC	1163.4	1163.2	1128.8
MACH NUMBER	0.000	0.053	1.000

PERFORMANCE PARAMETERS

Ae/At	11.335	1.0000
CSTAR, M/SEC	1741.3	1741.3
CF	0.0353	0.6483
Ivac, M/SEC	19768.8	2141.9
Isp, M/SEC	61.4	1128.8

MASS FRACTIONS

*CO 2.4949-1 2.4946-1 2.3695-1

*CO2 2.5328-1 2.5333-1 2.7299-1

COOH 3.9700-6 3.9597-6 2.4439-6

*H 2.0826-3 2.0825-3 1.8639-3

HCO 2.7552-6 2.7477-6 1.5513-6

*HCO+ 6.839-10 6.817-10 3.054-10

HO2 1.4489-4 1.4464-4 1.0328-4

*H2 5.2736-3 5.2732-3 4.9549-3

HCHO,formaldehy 2.6660-8 2.6573-8 1.3958-8

HCOOH 1.9296-7 1.9235-7 1.1117-7

H2O 2.4354-1 2.4356-1 2.5226-1

*H2O+ 2.601-10 2.592-10 1.129-10

H2O2 7.6428-6 7.6256-6 5.0641-6

*H3O+ 1.6696-8 1.6656-8 9.6022-9

*O 3.2971-2 3.2964-2 2.8837-2

*O- 6.017-10 5.994-10 2.519-10

*OH 8.0943-2 8.0921-2 7.3583-2

OH- 1.964 -9 1.956 -9 9.008-10

*O2 1.3225-1 1.3225-1 1.2845-1

*O2+ 3.577-10 3.566-10 1.585-10

O2- 2.208-10 2.198-10 8.835-11

O3 3.2321-7 3.2231-7 1.8216-7

* THERMODYNAMIC PROPERTIES FITTED TO 20000.K

NOTE. WEIGHT FRACTION OF FUEL IN TOTAL FUELS AND OF OXIDANT IN TOTAL OXIDANTS

Seeded Input File:

CEA analysis performed on Tue 10-Jan-2023 06:36:05

Problem Type: "Rocket" (Finite Area Combustor)

prob case=_____4532 ro equilibrium ions fac

!Mass Flux/Chamber Area, kg/sec-sqm:

mdot=20.23

```
# Pressure (1 value):
p,psia= 58

# Oxidizer/Fuel Wt. ratio (1 value):
o/f= 3.64

# You selected the following fuels and oxidizers:
reac
fuel C3H8            wt%= 99.5000
fuel Na              wt%=  0.5000
oxid O2              wt%=100.0000

# You selected these options for output:
# short version of output
output short
# Proportions of any products will be expressed as Mass Fractions.
output massf
# Heat will be expressed as siunits
output siunits
# Trace variable:
output trace=1e-10

# Input prepared by this script:/var/www/sites/cearun.grc.nasa.gov/cgi-bin/CEARUN/prepareInputFile.cgi

### IMPORTANT:  The following line is the end of your CEA input file!
end
```

Seeded Output File:

```
      NASA-GLENN CHEMICAL EQUILIBRIUM PROGRAM CEA2, FEBRUARY 5, 2004
            BY  BONNIE MCBRIDE AND SANFORD GORDON
    REFS: NASA RP-1311, PART I, 1994 AND NASA RP-1311, PART II, 1996

*******************************************************************************

### CEA analysis performed on Tue 10-Jan-2023 06:36:05

# Problem Type: "Rocket" (Finite Area Combustor)

prob case=_______________4532 ro equilibrium  ions  fac
```

```
!Mass Flux/Chamber Area, kg/sec-sqm:
mdot=20.23

# Pressure (1 value):
p,psia= 58

# Oxidizer/Fuel Wt. ratio (1 value):
o/f= 3.64

# You selected the following fuels and oxidizers:
reac
fuel C3H8             wt%= 99.5000
fuel Na               wt%=  0.5000
oxid O2               wt%=100.0000

# You selected these options for output:
# short version of output
output short
# Proportions of any products will be expressed as Mass Fractions.
output massf
# Heat will be expressed as siunits
output siunits
# Trace variable:
output trace=1e-10

# Input prepared by this script:/var/www/sites/cearun.grc.nasa.gov/cgi-bin/CEARU
N/prepareInputFile.cgi

### IMPORTANT:  The following line is the end of your CEA input file!
end

          THEORETICAL ROCKET PERFORMANCE ASSUMING EQUILIBRIUM

        COMPOSITION DURING EXPANSION FROM FINITE AREA COMBUSTOR

Pin =    58.0 PSIA
MDOT/Ac =    20.230 (KG/S)/M**2      Pinj/Pinf =  1.001551
CASE = _________________

         REACTANT                WT FRACTION      ENERGY      TEMP
                            (SEE NOTE)     KJ/KG-MOL      K
FUEL       C3H8                  0.9950000        0.000      0.000
FUEL       Na                    0.0050000        0.000      0.000
OXIDANT    O2                    1.0000000        0.000      0.000

O/F=    3.64000  %FUEL= 21.551724  R,EQ.RATIO= 0.992291  PHI,EQ.RATIO= 0.992291

             INJECTOR  COMB END  THROAT
Pinj/P          1.0000   1.0031   1.7214
P, BAR          3.9989   3.9866   2.3230
T, K          3319.55  3318.93  3188.33
RHO, KG/CU M    3.3132-1 3.3036-1 2.0365-1
H, KJ/KG         0.00003  -1.8746  -635.48
U, KJ/KG        -1206.97 -1208.59 -1776.18
G, KJ/KG        -40832.3 -40828.5 -39855.6
S, KJ/(KG)(K)    12.3006  12.3011  12.3011
```

M, (1/n)	22.868	22.868	23.240
(dLV/dLP)t	-1.07238	-1.07238	-1.06860
(dLV/dLT)p	2.3561	2.3563	2.3420
Cp, KJ/(KG)(K)	11.3209	11.3237	11.4693
GAMMAs	1.1184	1.1184	1.1142
SON VEL,M/SEC	1161.9	1161.7	1127.4
MACH NUMBER	0.000	0.053	1.000

PERFORMANCE PARAMETERS

Ae/At	11.350	1.0000
CSTAR, M/SEC	1739.1	1739.1
CF	0.0352	0.6482
Ivac, M/SEC	19769.0	2139.2
Isp, M/SEC	61.2	1127.4

MASS FRACTIONS

*e-	5.681-10	5.680-10	5.055-10
*CO	2.4708-1	2.4705-1	2.3452-1
*CO2	2.5384-1	2.5388-1	2.7358-1
COOH	3.9412-6	3.9309-6	2.4250-6
*H	2.0568-3	2.0567-3	1.8400-3
*H-	3.2169-9	3.2098-9	1.8641-9
HCO	2.7039-6	2.6966-6	1.5210-6
HO2	1.4573-4	1.4549-4	1.0392-4
HO2-	1.415 -9	1.410 -9	6.870-10
*H2	5.1951-3	5.1947-3	4.8787-3
HCHO,formaldehy	2.6062-8	2.5976-8	1.3630-8
HCOOH	1.9082-7	1.9022-7	1.0987-7
H2O	2.4271-1	2.4273-1	2.5139-1
H2O2	7.6575-6	7.6403-6	5.0747-6
*Na	8.2087-4	8.2109-4	8.4978-4
*Na+	2.8884-5	2.8873-5	2.4579-5
*Na-	6.220-10	6.207-10	4.050-10
NaH	2.6564-6	2.6523-6	1.9436-6
NaO	3.8402-5	3.8352-5	2.9992-5
NaOH	3.5256-4	3.5225-4	3.1957-4
*NaOH+	1.916-10	1.909-10	8.175-11
Na2	3.3564-9	3.3500-9	2.4404-9
Na2O	1.7042-9	1.6998-9	1.1453-9
Na2O+	1.073-10	1.070-10	5.620-11
Na2O2H2	2.061-10	2.054-10	1.387-10
*O	3.2998-2	3.2991-2	2.8864-2
*O-	8.1935-7	8.1778-7	5.1415-7
*OH	8.0795-2	8.0774-2	7.3450-2
OH-	2.6687-6	2.6640-6	1.8349-6
*O2	1.3391-1	1.3391-1	1.3014-1
O2-	3.0369-7	3.0296-7	1.8222-7
O3	3.2864-7	3.2773-7	1.8537-7

* THERMODYNAMIC PROPERTIES FITTED TO 20000.K

NOTE. WEIGHT FRACTION OF FUEL IN TOTAL FUELS AND OF OXIDANT IN TOTAL OXIDANTS